

Effect of flow confinement on the hydrodynamics of circular impinging jets: implications for erosion assessment

Seyed Mohammad Ghaneeizad ·
Joseph F. Atkinson · Sean J. Bennett

Received: 10 October 2013 / Accepted: 14 April 2014
© Springer Science+Business Media Dordrecht 2014

Abstract The fluid dynamics of a water jet impinging on a flat surface in confined conditions were studied using particle image velocimetry. The experiments were meant to replicate conditions expected in a jet erosion test (JET) designed to assess cohesive sediment erosion parameters in field applications. High-resolution two-dimensional velocity vectors were measured in a plane passing the jet centerline including free jet, impingement, and wall jet regions within a fixed-wall box. The general flow behavior in the free jet and wall jet regions is in good agreement with the behavior of impinging jets in an unconfined environment. Results show that the entrainment coefficient, however, is lower than values in unconfined conditions, lowering lateral spreading rates. The rate of momentum transfer also increases along the axial direction since the confinement causes secondary flow and recirculation in the box. Wall shear stress is calculated based on extrapolation of Reynolds shear stress and turbulent kinetic energy, where the latter procedure provides more consistent results with expected scour hole shape under an impinging jet. This wall shear stress distribution shows higher values near jet impingement in comparison to previously reported distributions, especially that formulated for the JET under unconfined conditions. The maximum value of wall shear stress is found to be about 2.4 times greater than the commonly accepted value in the literature, and also occurs at a position closer to the impingement point. The shear stress at the impingement point is also close to its maximum value, which is consistent with the expected scour hole shape beneath an impinging jet. These findings have important implications for the use of jet impingement theory to assess sediment erosion, especially in the application of the JET.

Keywords Impingement jet · Wall shear stress · Confinement · Soil erosion · Field apparatus

S. M. Ghaneeizad (✉) · J. F. Atkinson
Department of Civil, Structural, and Environmental Engineering, University at Buffalo,
Buffalo, NY 14260, USA
e-mail: sghaneei@buffalo.edu

S. J. Bennett
Department of Geography, University at Buffalo, Buffalo, NY 14261, USA

24 1 Introduction

25 Impinging jets play an important role in many industrial, mechanical, and environmental engi-
 26 neering processes such as heating, cooling, drying, rotorcraft brownout, headcut erosion, and
 27 discharge of pollutants in rivers, lakes, and oceans [1–3]. One of the practical applications
 28 of an impinging jet is in the assessment of soil erosion and erodibility. Many studies have
 29 employed an impinging jet to investigate the erodibility of soils and sediments in stream
 30 channels, dam embankments, and marine and estuarine environments [4–11], although as
 31 described below, these studies generally are based on results obtained in unconfined condi-
 32 tions, whereas the apparatus used for testing imposes confinement.

33 A submerged jet erosion test (JET) was designed for testing materials in the field [12, 13],
 34 and is now a developed ASTM standard used commonly around the world [14]. The goal
 35 of in situ testing devices such as this is to deliver an accurate estimation of soil erodibility
 36 without disturbance to the material that may occur in moving a soil sample to the laboratory.
 37 Sample disruption due to transport is a potential problem in other testing devices such as the
 38 rotating cylinder apparatus [4], flume experiments [15], drill hole apparatus [16], Sedflume
 39 [17], or the erosion function apparatus [18]. The JET can be applied for either horizontal
 40 (stream bed) or angled (side channel) surfaces [12, 13]. The device uses a constant head
 41 jet mounted inside an enclosed cylinder that defines the test space. The volume of soil
 42 removed under the impinging jet (as the scour hole deepens) is determined using a point
 43 gauge. Based on the scour hole depth, the rate of erosion is determined. Jet impingement
 44 theory then is applied to determine the shear stress on the soil surface, and the critical
 45 tractive shear stress and the soil's erodibility coefficient are derived. This device has been
 46 used in many locations worldwide to quantify the erodibility of soils, providing researchers
 47 with a tool to evaluate in situ erosion potential [19, 20]. Contemporary research, however,
 48 is still aimed at developing better understanding of the phenomena involved with the JET
 49 [21].

50 The equations used in conjunction with the JET are based on jet impingement theory,
 51 which considers an axisymmetric, circular, impinging jet with three distinct regions of flow
 52 as shown in Fig. 1 [22]. The first is the free jet region (I), where the impingement plane has
 53 no effect. The second is the impingement region (II), where the jet significantly decelerates
 54 as it approaches the impingement plane, and then is directed from the axial direction to the
 55 radial direction. After some radial distance from the impingement point the wall jet region
 56 (III) develops.

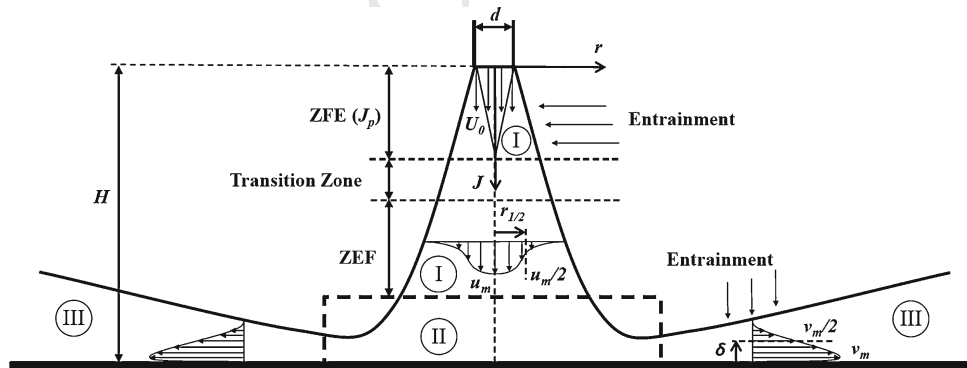


Fig. 1 Axisymmetric impinging jet and three regions of interest (after [22])

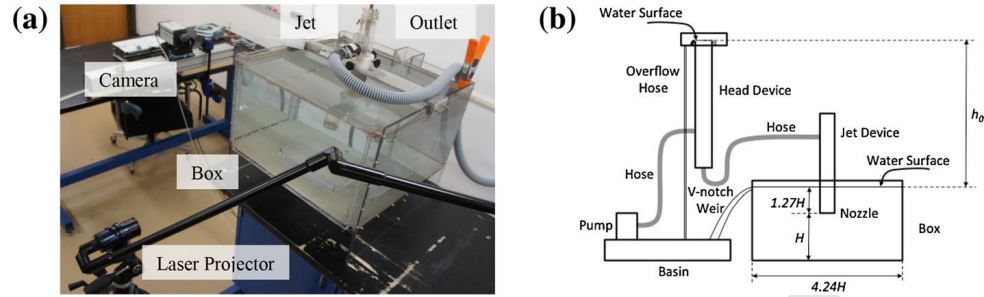


Fig. 2 **a** Laboratory setup including laser projector, camera, jet device, box, and pump, and **b** Impinging jet setup sketch

Using the JET to assess soil erosion requires an accurate understanding of jet hydrodynamics. Although many researchers have studied impinging jets, a number of questions arise in the application of impinging jet theory to assess sediment entrainment. For example, even when the bed is flat as at the beginning of the test, Phares et al. [23] have shown that the commonly accepted distribution of applied bed shear stress as determined by Beltaos and Rajaratnam [22], and assumed by Hanson [12], was derived incorrectly (see below). Also, the real-time applied shear stress is not constant when the jet is eroding the surface and the surface is no longer flat (e.g., [24]). Furthermore, a review of impinging jet studies in the literature reveals that (1) all studies have been done with an air jet except Hanson et al. [25], (2) no studies have been conducted using the actual JET employed in soil erosion assessment, and (3) previous work has not considered the possible effects of the confined environment on jet hydrodynamics and the scaling arguments for velocity and impingement shear stress. This study focuses on this last issue and investigates the flow characteristics of an impinging jet within a confined space similar to the JET, so that the results can be used to verify the relations and coefficients employed to quantify sediment erosion indices in the field. The main objectives of this paper are (1) to characterize the time-mean and turbulent flow of a circular impinging jet within a confined volume, (2) to quantify the shear stress distribution on a flat bed surface at impingement and with distance away from this point, and (3) to critically assess the application of an impinging jet for sediment erosion measurement and characterization.

2 Experimental methods

Experiments were conducted using a box of size $670 \times 670 \times 400$ mm ($4.24H \times 4.24H \times 2.53H$), where $H = 158$ mm is the impingement height). The confinement ratio (box area to nozzle area) was 13,950, and a V-notch weir on the left side of box (viewed from the camera position) provided the outlet for the box. The laboratory setup included a particle image velocimetry (PIV) system, test box, jet device, injecting syringe, basin, and pump (Fig. 2).

The conditions for the JET in the field were reproduced in the laboratory using a jet with a 6.4-mm nozzle diameter d_0 . The test volume here, however, was slightly larger than the JET, and flat vertical surfaces were used (in contrast to the cylindrical volume of the JET) to facilitate the acquisition of PIV data. Water was pumped from a basin to a constant head device to produce the jet (see Fig. 2b). A syringe was used to inject a solution of seed particles into the water just before the nozzle, since the main interest was in the jet flow and not the

Table 1 General properties of the jet where U_0^* is the ideal nozzle velocity (no losses), U_0 is the measured nozzle velocity, K is the loss coefficient, Q_0 is the nozzle discharge, and \dot{M}_0 is the nozzle rate of momentum transfer

Experiment	h_0 (m)	d_0 (m)	U_0^* (m/s)	U_0 (m/s)	K	Q_0 (m ³ /s)	\dot{M}_0 (N)
Run 1 (Low head)	0.735	0.0064	3.80	3.67	0.07	104×10^{-6}	0.385
Run 2 (High head)	1.487	0.0064	5.40	5.27	0.05	149×10^{-6}	0.785

ambient fluid. The experiments were done using two heads h_0 : a low head (Run 1) of 735 mm, and a high head (Run 2) of 1,487 mm. Using Bernoulli's equation, the ideal (no losses) nozzle velocities U_0^* for Run 1 and Run 2 were 3.80 and 5.40 m/s, respectively. These and other experimental conditions are summarized in Table 1.

The PIV system was used to measure the two-dimensional velocity field focusing on the plane passing the jet centerline (Fig. 1), and was measured in five separate zones: (1) the near-field of the free jet region, (2) the far-field of the free jet region, (3) the impingement region, (4) the near-field of the wall jet region, and (5) the far-field of the wall jet region. This procedure allowed greater accuracy and spatial resolution than could be obtained with a single image of the entire flow. Note that the wall jet results were developed for the right side of the jet, opposite to the discharge outlet. In addition, small discontinuities sometimes arose when combining two data sets that overlapped slightly in space (see below). The spatial resolution of Zones 1 and 2 were 0.9 and 2.1 mm, respectively. The resolution of Zone 1 was chosen to be higher than that of Zone 2 because of high velocity gradients near the nozzle. A high spatial resolution of 0.6 mm also was chosen for Zones 3, 4, and 5 because of interest in the wall shear stress. The jet was allowed to run for at least one hydraulic residence time (test box volume/jet flow) before any measurements were taken, and preliminary tests confirmed there were no substantial changes in jet characteristics after that time. The camera was able to capture up to 500 images in memory for each data collection period. Because of laser warm-up time, variation in particle injection, and other experimental issues, about 350–450 images were considered valid for each run. The trigger rate of the camera was set to 80 Hz, and 13 data collection periods for each zone were captured for averaging purposes. Out of those periods, 10 or 11 data collection periods in Zones 1 and 2, and 5 or 6 data collection periods in Zones 3, 4, and 5 typically were identified as valid. The smaller number of valid images for measurements close to the wall is thought to be due to interferences related to the presence of the wall. The total lengths of time of captured flow used in the analyses for the free jet and wall jet regions were thus 60 and 30 s, respectively. Exposure time for each laser frame and the time between pulses were set at 120 and 100 μ s, respectively. Dynamic Studio Version 13.4 software was used to analyze images. The software was able to process images and build 2D-vector maps in the domain. Spatial calibration was accomplished using a target of 270×190 mm with white dots and black background, and an interrogation area of 16×16 pixels was chosen for all zones except Zones 1 and 2 of Run 2 which have an interrogation area of 32×32 pixels. Based on Willert [26], the uncertainty of PIV displacement measurements for in-plane components is on the order of 0.06 pixel, which is equivalent to 0.28 mm/s (0.56 mm/s) for Zone 1, 0.63 mm/s (1.26 mm/s) for Zone 2, and 0.18 mm/s (0.18 mm/s) for Zones 3, 4, and 5 of Run 1 (Run 2). Processed data were exported as text files and analyzed using user-defined codes in MATLAB R2012b.

3 Results

To characterize jet behavior, the jet properties are first compared to those reported in the literature for the free jet, impingement, and wall jet regions. Note that d_0 is the only scaling length for the free jet region, while for the impingement and wall jet regions d_0 and H are alternative scaling lengths, where $H/d_0 = 24.7$ for the present tests. For the following plots that have alternative distance axes, the bottom axis is the distance normalized using the default scaling length for the plots, and the top axis is an additional scaled distance to better understand the relation between free and wall jet regions.

3.1 Free jet (Region I)

The free jet definition applies to neutrally buoyant turbulent jets diffusing in an unbounded environment (e.g. [27]). Although the present case is an impinging jet in a bounded environment, results were compared to the behavior of free jets to identify any differences between unconfined free jets and the present jet. A submerged free jet has two distinct sub-regions [28]. The first sub-region is the zone of flow establishment (ZFE), also known as the potential core, and extends from the jet origin ($J = 0$, where J is axial distance from the nozzle) to a point along the jet axis where the mixing region on all sides of the jet has penetrated to the centerline of the jet ($J = J_p$, where J_p is the length of the potential core, see Fig. 1). Hanson et al. [25] found $J_p = 6.3d_0$. In this region, the time-averaged centerline velocity \bar{u}_m , which also is the local maximum axial velocity in free jets, is constant and equal to the nozzle exit velocity U_0 . The other sub-region is the zone of established flow (ZEF), which for impinging jets extends to a point where the boundary begins to affect the velocity magnitude and direction. In this region, \bar{u}_m decreases with increasing J , and the cross-sectional velocity profiles have a Gaussian distribution. Typically, the ZEF extends to $J/H = 0.86$ [22]. In order to obtain high-resolution data, free jet measurements were divided into near-field and far-field regions and separate measurements were performed for each. Any apparent discontinuities in plots at $J/d_0 = 8.7$ are due to joining those datasets.

3.1.1 General observations

The nozzle velocities U_0 are given in Table 1. These measured velocities are just 3.4 and 2.5 %, respectively, lower than the theoretical computed velocities assuming no losses. Thus, the head loss coefficients K for Run 1 and Run 2 are 0.07 and 0.05, respectively. These values lead to a discharge coefficient C for the nozzle ($U_0 = C \frac{\pi}{4} d_0^2 \sqrt{2gh_0}$) of about 0.97 for both runs, which confirms the range of 0.95 to 1.00 reported by Al-Madhhachi et al. [29] for the JET. Measured U_0 is used to scale other parameters in the free jet and wall jet regions. Comparing Run 1 and Run 2, both free-jets evolved in almost the same way with increasing distance from the nozzle.

3.1.2 Length of the potential core

The length of the ZFE was used by Hanson et al. [20] to relate the maximum wall shear stress to the maximum stress at the nozzle, so its value is important in how data are presented, as discussed further below. This length was found to be $J_p = 2.3d_0$ for both runs (compare with Hanson's [24] value of $6.3d_0$), and even at $J/d_0 = 5$ the variation of \bar{u}_m from U_0 is only about 10 %.

11

3.1.3 Centerline velocity decay

In the ZEF, the mean centerline velocity decays as [30–32]

$$\frac{\bar{u}_m}{U_0} = C_d \left(\frac{J - J_0}{d_0} \right)^{-1} \quad (1)$$

where C_d is the diffusion coefficient and J_0 is a virtual origin for the velocity profile of the ZEF. Both C_d and J_0 depend on the exit conditions [33]. The reported range for C_d is 5.8 to 7.4, with a commonly accepted average of 6.3 [22]. Hussein et al. [31] proposed $J_0 = 4d_0$. Many studies, however, have suggested that the virtual origin may be taken as zero because it is much smaller than J [28]. For a highly confined free jet in a pipe, Liu et al. [34] found a slightly modified form of Eq. (1) was applicable,

$$\frac{\bar{u}_m}{U_0} = C_d \left(\frac{J}{d_0} \right)^{-1} - 1.4 \frac{d_0}{D} \quad (2)$$

where D is the diameter of the confining pipe. In this study, D is defined as the equivalent diameter of the confining box, so that d_0/D is 0.008.

The present centerline velocity data do not agree with (Eq. 2), although there is good agreement with Eq. (1) for distances greater than $J/d_0 = 4.6$ (Fig. 3; note that the vertical axis is inverted from Eq. 2, to be consistent with previous studies). The values of C_d and J_0 in Eq. (1) for the present study, however, are not the same as suggested for unconfined jets. The free jet is fully developed before entering the impingement region and is affected by the impingement plane at $J = 21.2d_0 \cong 0.860H$ for both runs. The fitted decay line was calculated using the centerline velocity in the ZEF for $J/d_0 = 4.6$ –21.2 for both runs. The virtual origins of the velocity profile were found to be $J_0/d_0 = -2.8$ and $J_0/d_0 = -2.9$ for Run 1 and Run 2, respectively – although J_0 is assumed as 0 below, these values are reported here to make the data reproducible for future studies. The diffusion coefficient C_d was found to be 7.9 and 7.6 for Run 1 and Run 2, respectively, somewhat greater than in the range of 5.8–7.4 noted above. Figure 3 shows that for the conditions of this apparatus, the centerline velocity starts to decay in a shorter distance from the nozzle than for ideal free jets. These differences are believed to be a result of confinement on the jet as discussed below.

Assuming $J_0 = 0$ in Eq. (1) and $\bar{u}_m = U_0$ at $J = J_p$, Hanson et al. [20] wrote

$$J_p = C_d d_0 \quad (3)$$

As can be seen in Fig. 3, although Eq. (1) predicts the centerline velocity in the ZEF, it is not valid close to the potential core, and there is a significant difference between measured and predicted velocities at $J = J_p$. Actually, there is a transition zone (TZ) between the ZFE and ZEF ($J/d_0 = 2.3$ –4.6 in the present case; see Fig. 3) where characteristics of neither zone apply. The centerline velocity decays by about 9 % in the TZ. By ignoring this transition length, Eq. (3) was suggested by Hanson et al. [20] to determine J_p , while it is more accurate to say this equation gives the total length of the ZFE and the TZ. Note that although J_p was found to be $2.3d_0$ in the present case, it could be a function of parameters such as confinement ratio and nozzle properties.

3.1.4 Lateral spreading rate

As the distance from the nozzle increases, more ambient fluid is entrained across the jet boundary, and the jet width increases. The jet nominal boundaries are usually specified by

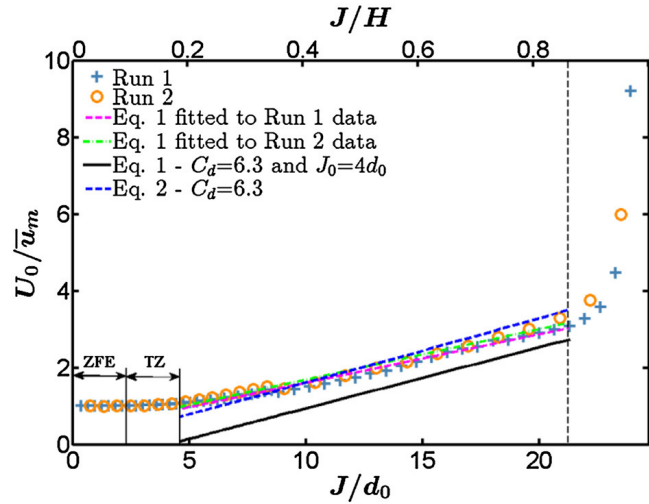


Fig. 3 Centerline velocity decay as a function of distance from the nozzle for Regions I and II (vertical dashed line indicates the boundary between Regions I and II, $J/H = 0.86$). The zone of flow establishment (ZFE) and the transition zone (TZ) are shown on the figure

the location where the time-mean axial velocity \bar{u} is an arbitrary fraction of the centerline velocity ($1/e$, or more usually $1/2$, [35]). Lateral spreading in unconfined free turbulent jets has been shown to be approximately linear and can be expressed as [36]

$$\frac{r_{1/2}}{d_0} = C_u \left(\frac{J - J'_0}{d_0} \right) \quad (4)$$

where $r_{1/2}$ is the jet half-width, defined by the location where the time-mean axial velocity is $1/2$ of the time-mean centerline velocity, $C_u = dr_{1/2}/dJ$ is the spreading rate, and J'_0 is the virtual origin for the lateral spreading rate. Values for C_u have found to be 0.107 [37] or 0.105 [38].

The free-jet half-width is shown in Fig. 4 for the two experimental runs. Although the lateral spreading of neither run is purely linear, a best fit line through the data in the ZEF ($J/d_0 = 4.6$ to 21.2) gives values of 0.066 and 0.076 for C_u , and values of -2.8 and -1.6 for J'_0/d_0 in Run 1 and Run 2, respectively. The average spreading rate for the two runs is about 33 % less than the measurements by Papanicolaou and List [37] and Hongwei [38], indicating less entrainment as the jet penetrates into the medium, as discussed further below.

3.1.5 Axial velocity distribution

A self-similarity solution to the equation of motion, which also has been shown experimentally, gives the radial distribution of axial velocity for axisymmetric free jets in unconfined conditions as [22]

$$\frac{u}{\bar{u}_m} = e^{-0.693\eta_u^2} \quad (5)$$

where $\eta_u = r/r_{1/2}$ and r is the radial distance from the jet centerline. Figure 5 shows that the present results are in good agreement with the self-similarity profile not only in the ZEF but also in the impingement region very close to the bed, although there is some additional spreading for the profile closest to the bed ($J/H = 0.95$).

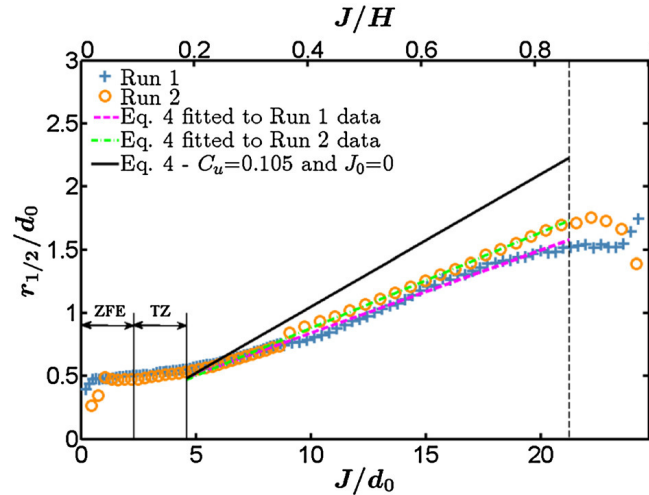


Fig. 4 Free jet half-width for Run 1 and 2 compared to that in unconfined conditions (vertical dashed line indicates the boundary between Regions I and II, $J/H = 0.86$). The zone of flow establishment (ZFE) and the transition zone (TZ) are shown on the figure

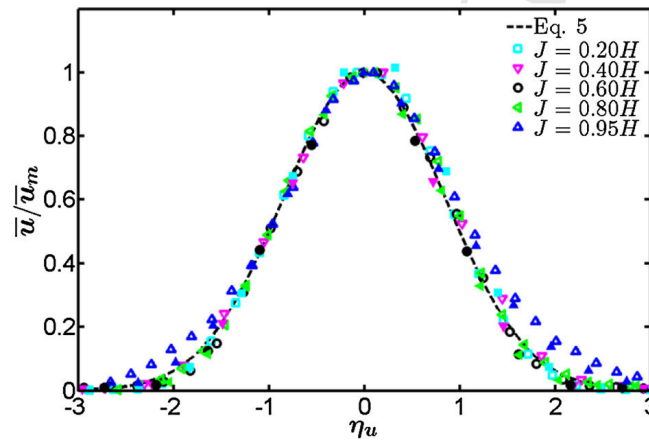


Fig. 5 Free jet self-similarity conditions (Run 1: open symbols; Run 2: filled symbols)

232 3.2 Impingement region (Region II)

233 The impingement region of a circular jet has been studied extensively [39–43]. In this region,
 234 the impingement plane affects the jet flow, and the flow becomes parallel to the surface at the
 235 end of this region. For large impingement heights $H > 8.3d_0$ [44], the flow is fully developed
 236 before entering the impingement region, and the critical flow parameters are U_0 and d_0 . The
 237 characteristic length scale for the impingement region length, and the pressure and shear
 238 stress distributions on the wall in this region is H [22,45]. Centerline velocity data (Fig. 3)
 239 indicate that the wall affects the flow at $J/H = 0.86$, which is taken here as the beginning
 240 of the impingement region.

241 Reynolds stresses, including shear stress $\overline{u'v'}$ and normal stresses $\overline{u'^2}$ and $\overline{v'^2}$, in the axial
 242 and radial directions, respectively, were not affected by the wall as much as the mean velocity
 243 at the beginning of the impingement region. To assess the impact of the impingement wall

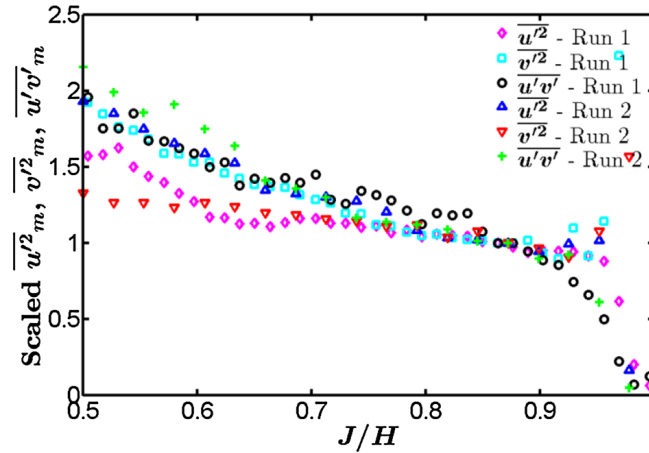


Fig. 6 Local maximum turbulence stresses scaled by their respective values at $J/H = 0.86$

on the Reynolds stresses, local maximum stresses $\overline{u'^2}_m$, $\overline{v'^2}_m$, and $\overline{u'v'}_m$ were normalized by their respective values at $J/H = 0.86$. All three stress scales decrease at relatively low rates as the jet diffuses from the nozzle to the impingement plane, but $\overline{u'^2}$ and $\overline{u'v'}$ decline rapidly in the vicinity of the wall (Fig. 6). As streamlines turn from the vertical to horizontal direction in the impingement region, $\overline{v'^2}$ increases close to the boundary. The wall affects $\overline{u'^2}$, $\overline{v'^2}$, and $\overline{u'v'}$ at $J/H = 0.96, 0.91$ and 0.92 , respectively, causing decreasing $\overline{u'^2}$ and $\overline{u'v'}$ and increasing $\overline{v'^2}$ for larger J/H . For unconfined conditions the stresses are affected by the wall at $J/H = 0.96$ [41].

3.3 Wall jet region (Region III)

The impingement region ends and the wall jet region starts where the excess stress on the wall approaches zero and the static pressure becomes equal to the ambient pressure. This transition occurs at $r/H = 0.22$ in an unconfined environment [22]. Wall jet flow depends on H even at large radial distances from the impingement point for large impinging heights ($H > 8.3d_0$) [46]. Similar to the above, any discontinuities in plots at $r/H = 0.4$ are due to joining two datasets collected for this region in post-processing.

3.3.1 Wall jet velocity distribution

It has been shown that the velocity distribution in the wall jet region can be described by a self-similarity function [35, 47],

$$\frac{v}{\bar{v}_m} = 1.48 \left(\frac{z}{\delta} \right)^{1/7} \left[1 - \operatorname{erf} \left(0.68 \frac{z}{\delta} \right) \right] \quad (6)$$

where \bar{v}_m is the (time averaged) local maximum of radial velocity, z is the vertical distance from the impingement wall, and the length scale δ is the jet half-width, which is taken as the value of z where the radial velocity is $0.5\bar{v}_m$ (note that there are two locations where $v = 0.5\bar{v}_m$; here the farther one from the wall is considered). Measured radial velocity distributions follow this self-similarity profile in the wall jet region, verifying the overall agreement to wall jet behavior as indicated by Eq. (6) (Fig. 7a). The self-similarity profile is valid for $r/H \geq 0.15$.

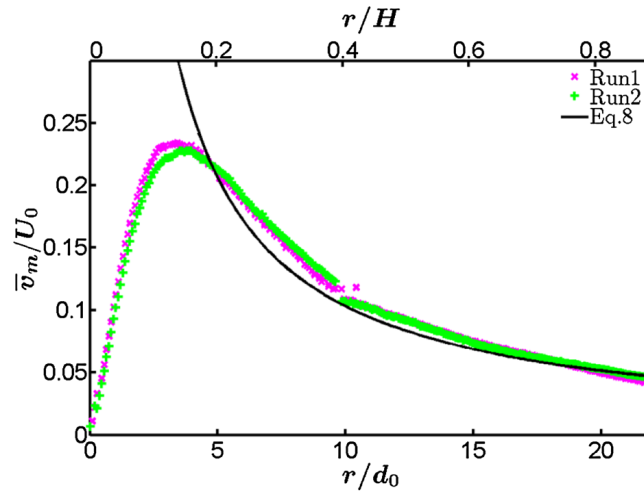


Fig. 7 Wall jet region characteristics: **a** radial velocity self-similarity (Run 1: open symbols; Run 2: filled symbols), **b** length scale (wall jet half-width), and **c** velocity scale (local maximum radial velocity)

3.3.2 Velocity and length scales

The length scale δ [46] and the velocity scale \bar{v}_m [35] are defined for an unbounded wall jet as

$$\frac{\delta}{H} = 0.098 \left(\frac{r}{H} \right)^{0.9} \quad (7)$$

$$\frac{\bar{v}_m}{U_0} = \frac{1.03}{r/d_0} \quad (8)$$

The present results show that the minimum value for δ (equal to $0.61d_0$) occurs at $r/H = 0.22$, and it increases for greater r (Fig. 7b). Although it follows the nearly linear trend of Eq. 7 for $r/H \geq 0.31$, the values are smaller and shifted to the right (Fig. 7b), showing that the wall jet in confined conditions is not as wide as in unconfined conditions. To account for this shift, Eq. (7) can be modified by adding a virtual origin as

$$\frac{\delta}{H} = 0.098 \left(\frac{r}{H} \right)^{0.9} - r_0 \quad (9)$$

where r_0 is a non-dimensional virtual origin and here is found to be 0.007. In a confined volume, the entrainment is limited by the boundaries and the existence of secondary flow. This lower entrainment rate results in a lower lateral spreading and a thinner jet. The wall jet velocity scale follows the overall behavior described by Eq. (8). Its maximum value occurs at $r/H = 0.14$, where the wall jet is not yet developed (Fig. 7c). As previously noted, Beltaos and Rajaratnam [22] proposed that the wall jet region starts at $r/H = 0.22$. Although the minimum jet half-width occurred at $r/H = 0.22$, the wall jet is not fully developed in the present study until $r/H = 0.27$, where the velocity normal to the wall becomes zero.

3.3.3 Reynolds shear stress behavior near wall

The maximum magnitudes of Reynolds shear stress occur close to the wall (Fig. 8a). The location of the local maximum occurs at $0.24d_0$ above the bed near the impingement point,

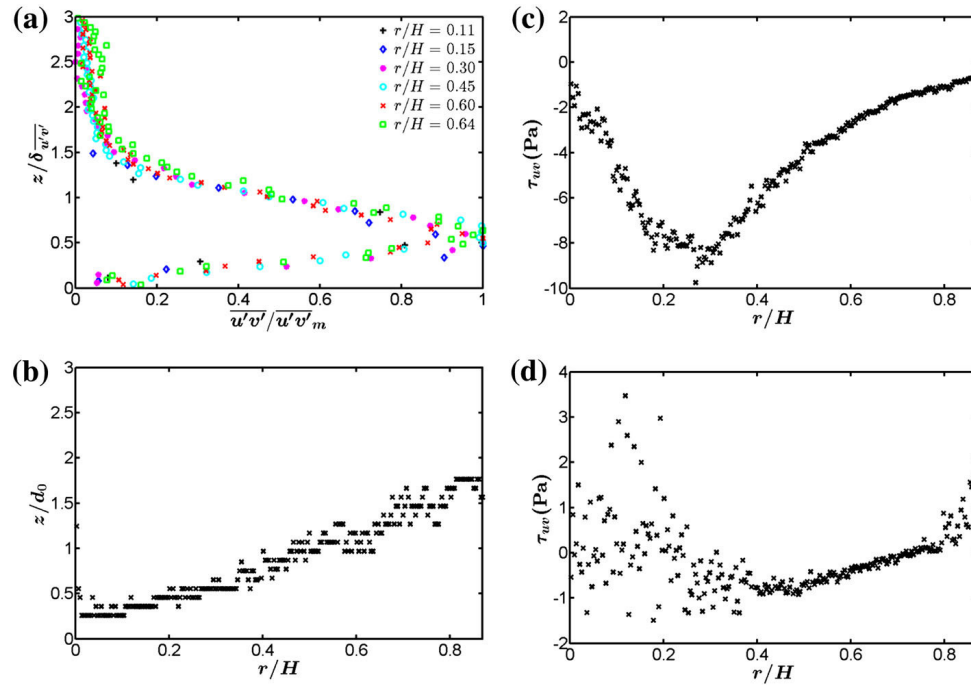


Fig. 8 Reynolds shear stress characteristics for Run 1: **a** scaled Reynolds shear stress profiles (length scale $\delta_{u'v'}$ is the jet half-width based on $u'v'$ profiles, taken as the value of z where $u'v'$ is $0.5u'v'_m$), **b** location of local maximum (distance from the wall), **c** local maximum value of Reynolds stress, and **d** measured Reynolds stress at the closest measurement point to the wall (0.4 mm above the wall)

and then moves farther from the wall with greater radial distance (Fig. 8b). Even far from the impingement point, the local maxima occur at distances less than $2d_0$ from the wall. The stresses are negative by convention. The magnitude of these local maxima increases with r , and reaches a peak at $r/H = 0.26$ (Fig. 8c). The measured Reynolds stresses at the closest position to the wall (0.4 mm above the wall) are shown in Fig. 8d. Near the impingement point up to a radial distance of $0.40H$, the measured values vary between -1.5 and 3.5 Pa, assuming water density is 1000 kg/m^3 . This large range of values casts doubt on the utility of using the near-bed Reynolds stress measurements to find the total wall shear stress.

4 Discussion

Results demonstrate that the free jet and wall jet flow of the JET follow the overall behaviors observed in previous studies for air jets in unconfined environments, but several important differences are found. Transport of momentum and variation of mass flux along the jet are considered in this section, followed by a discussion of the distribution of the wall shear stress and its application to soil erosion characterization.

4.1 Momentum and entrainment

The nozzle discharge Q_0 and rate of momentum transfer M_0 of the jet can be found based on the nozzle velocity U_0 and diameter d_0 (see Table 1). As the jet moves into the box, the flow

discharge increases because of entrainment of ambient fluid. The entrainment rate is related to the centerline velocity by an entrainment coefficient α ,

$$\frac{dQ}{dJ} = \alpha (2\pi b' \bar{u}_m) \quad (10)$$

where b' is the jet full-width [48], defined in this study by assuming the jet extends to the location where the axial velocity is 1.5 % of centerline velocity. This percentage is chosen to include as much of the actual jet momentum as possible. Many studies have provided measured or calculated values of the entrainment coefficient. For a free jet entering an unconfined volume, proposed values vary between 0.065 and 0.080 [31, 49–51].

The JET in field applications confines the jet in a cylinder, so the jet enters a finite volume and excess fluid discharges at the top of the cylinder [13]. This setup introduces two issues not present in unconfined tests: (1) recirculation of fluid because of the enclosure, and (2) flows caused by fluid exiting the experimental volume. The one main difference between the present test setup and the JET is that the experimental environment employed here is rectangular to avoid problems using PIV on a curved surface, whereas the JET is cylindrical. The box also encloses a larger volume, so any effect of confinement seen here is likely to be stronger in the JET.

To study the effect of confinement and the outlet condition, the right and left sides of the jet for Run 1 are considered separately. The velocity vector map reveals the existence of strong secondary flows in the box (Fig. 9), which has been observed and discussed in previous studies on confined jets [34, 52–54]. This plot also shows there is an effect of the outlet location as indicated by the asymmetric ambient flow circulation. However, details of this effect are beyond the scope of the present study, and in any case the ambient flow is not fully resolved here. Any observed differences between left and right sides of the jet can be attributed to the effects of the outlet location. The confining walls of the box cause the wall jet to turn upward, which drives circulation of flow from the wall jet region back to the free jet region. This turning begins at $r/H = 0.27$ on the right side of the wall jet, and $r/H = 0.18$ on the left side of the wall jet (Fig. 9). The more intensive effect of the confinement on the left side is associated with outflow conditions. Using PIV images and velocity vector maps, the jet axis, defined as the loci of local maximum of axial velocity, was verified to be orthogonal to the wall boundary to ensure that this asymmetric behavior was not due to any unintended physical deviation of the jet axis from vertical. The jet width on either side of the jet axis increases with the same slope at first, but gradually the growth rate for the left-hand side decreases and deviates from the linear trend (Fig. 10). The right side, however, extends linearly to the point where the jet enters the impingement region, and the deviation can be seen after $J/H = 0.87$ (Fig. 10).

As the jet enters the box, entrainment linearly increases the jet flow rate from the initial value at the nozzle up to a maximum near the boundary of the free-jet and impingement region at $J/H = 0.89$ and 0.82 for the right and left side, respectively. The initial flow rate for both sides is the same and increases at the same rate up to about $J = 5d_0$, where the effect of confinement and other conditions such as the position of the outlet differentiate the right and left side of the free jet (Fig. 11). It can be seen that the flow rate on the left-side is less than on the right-side. Figure 12 shows the variation of α along the jet calculated using two methods: (1) using Eq. 10 with Q calculated by the integration of axial velocities over the respective side area, which is determined by the jet full width, and (2) using $\alpha = u_e/u_m$ [35] with measured entrainment velocity u_e , taken as the horizontal velocity component at the edge of the jet where $r = b'$. The entrainment coefficient of the jet according to the second method is more than 85 % less than the above-mentioned values for non-confined

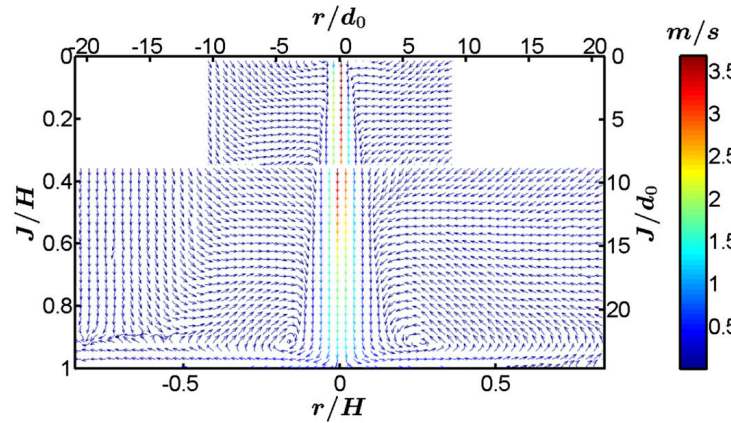


Fig. 9 Two-dimensional velocity field for Run 1 by joining measurements in Zones 1 and 2. Nozzle is located at $r = 0$ and $J = 0$. Note that the test box edges are at $r = 2.12H$ although the vectors are affected even before $r = H$

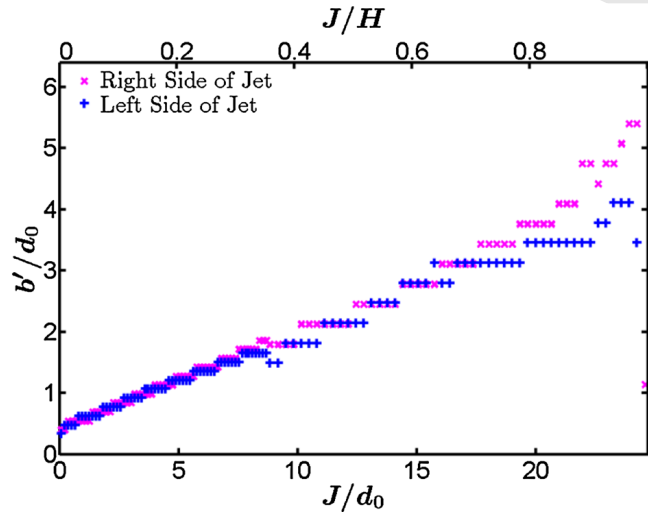


Fig. 10 Free jet full-width for the left and right sides for Run 1, calculated assuming the jet boundary is where the axial velocity is 1.5 % of centerline velocity

conditions (Fig. 12). Confinement limits the available volume of fluid to entrain and decreases the spreading rate of the jet. These limited entrainment rates and consequently low jet width also were observed in previous studies of confined jets [55–57].

The rate of momentum transfer \dot{M} on each side of the jet can be determined by integrating momentum flux over each (left and right sides) respective cross-section area,

$$\dot{M} = \int_{r=0}^{r=b'} r \pi \rho (\bar{u}^2 + \overline{u'^2}) dr \quad (11)$$

where the total momentum transfer rate is the sum of Eq. (11) evaluated for the left and right sides of the jet. In the case of momentum-conserving jets, \dot{M} at any distance from the nozzle must equal the value at the nozzle in the absence of imposed pressure gradients, and

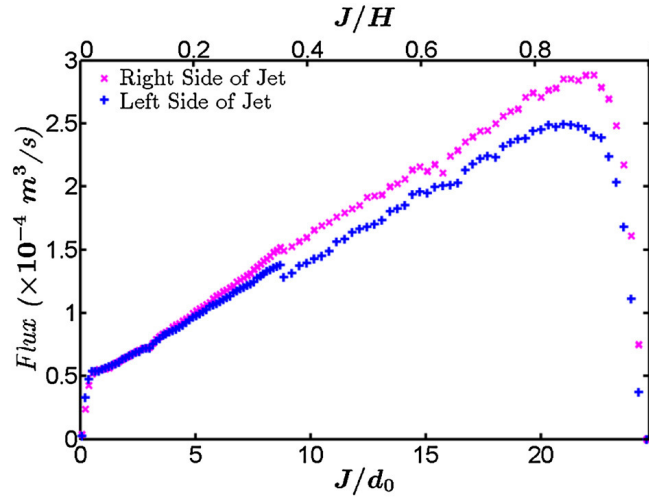


Fig. 11 Free jet flow rate for the left and right sides for Run 1, calculated using jet full-width

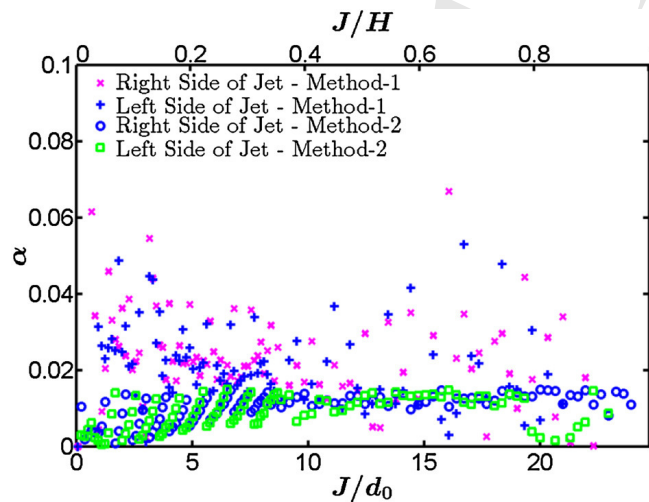


Fig. 12 Free jet entrainment coefficient (α) for the left and right sides for Run 1 (Method-1: based on Eq. 10 using calculated flow rate; Method-2: based on $\alpha = u_e/u_m$ using measured entrainment velocity at the jet boundary $r = b'$)

the entrainment that occurs in the radial direction does not change the axial momentum [58]. Figure 13 shows that the rate of axial momentum transfer varies along the jet axis. This effect is seen on both sides of the jet, but with different magnitudes. Initially, \dot{M} is the same for both sides and close to $0.5\dot{M}_0 = 0.19N$. Also, \dot{M} on both sides increases from the nozzle up to $J = 8.1d_0 = 0.33H$, and then decreases slightly up to $J = 0.85H$, where it is substantially affected by the impingement plane. The left-side \dot{M} , however, is less than the right-side value except when $J < 3d_0$. At first glance it appears unusual that \dot{M} should increase with increasing distance from the nozzle, but this increase can be explained by considering the recirculation in the box. In other words, the entrained flow does not enter the jet with zero axial velocity; rather, it adds to the axial momentum of the free jet. It is obvious that high pressure gradients close to the impingement plane are responsible for the decline of \dot{M} in that

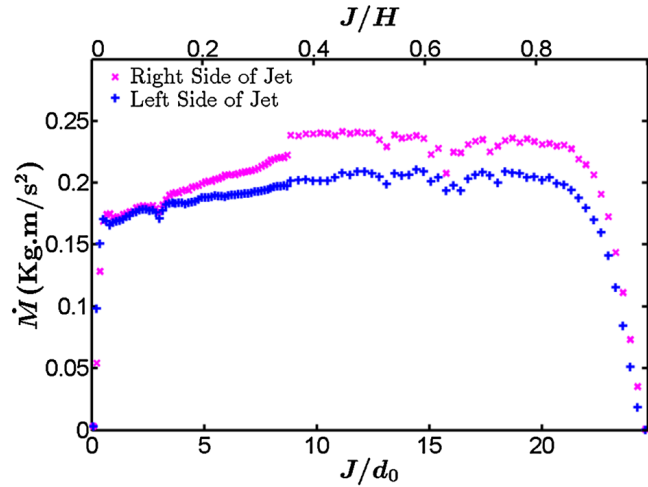


Fig. 13 Rate of momentum transfer for the left and right sides of the free jet for Run 1

region. As there are many unknowns such as pressure gradients, gain of momentum across the jet boundary, and its loss, performing a complete momentum balance through the jet is not possible. It is generally accepted, however, that the jet momentum in the axial direction is not conserved through the whole length of the jet [59–61], especially in the confined conditions due to recirculation effects [62].

These observations of relatively low jet width and high momentum transfer rates represent significant effects of confinement on the jet behavior. These results demonstrate that the recirculation and return flow in a confined environment increase the momentum and decrease the free jet width. These are consequences of entrainment provided by the recirculated flow instead of being in an infinite environment in which recirculation does not exist [63]. Experimental measurements of Karimipناه [48] showed that when the ratio of the room area to the nozzle area was larger than 10,400, the jet momentum was close to that of the unconfined jet. In the present study, this ratio is somewhat larger, around 13,950, but the confinement still affected the jet momentum. This could be due to the differences in experimental setups (Karimipناه considered a compressed air jet and two ceiling outlets).

4.2 Shear stress distribution on the impingement plane

Based on a solution to the equation of motion in the axial direction, Beltaos and Rajaratnam [22] suggested the shear stress distribution at the impingement plane is

$$\frac{\tau}{\tau_m} = 0.18 \left(\frac{1 - e^{-114\lambda^2}}{\lambda} \right) - 9.43\lambda e^{-114\lambda^2} \quad (12)$$

where $\lambda = r/H$ is the dimensionless distance from the impingement point, and τ_m is the maximum shear stress given by

$$\tau_m = 0.16 \frac{\rho U_0^2}{(H/d_0)^2} \quad (13)$$

and τ_m occurs at $\lambda = 0.14$. Examining a water jet impinging on a smooth planar surface, Hanson et al. [25] found the wall shear stress distribution to be similar to that of an air jet, with shear stress also given by Eqs. (12) and (13). Hanson and Cook [13] assumed the maximum

shear stress on the bed causes the maximum scour depth beneath the JET, and defined the maximum shear stress,

$$\tau_m = C_f C_d^2 \frac{\rho U_0^2}{(J_s/d_0)^2} \quad (14)$$

where J_s is the distance from the nozzle to the soil surface at the jet centerline, which is initially $J_s = H$ and increases to $J_s = H_e$ at equilibrium where τ_m is equal to critical shear stress τ_c , C_f is the coefficient of friction equal to 0.00416, and C_d is 6.3, resulting in $C_f C_d^2 = 0.16$ (see Eq. 13). Values of C_f and C_d were determined based on direct measurements of shear stress on a smooth surface beneath an impinging jet using a hot-film probe by Hanson et al. [25]. In this study, $C_s = C_f C_d^2$ is defined as the maximum shear stress coefficient for easier comparison of maximum wall shear stress.

The accuracy of any sediment erodibility assessment using the JET is highly dependent on the accuracy of estimation of applied shear stress by the jet on the sediment surface (Eq. 14). This equation has been developed for a jet impinging on a smooth, flat surface. The scour hole formation in the field results in a curved, rough surface. In addition, the assumption of the maximum scour hole caused by the maximum shear stress is not consistent with the off-axis location of maximum shear stress in Eq. (12). In addition, although Eq. (12) appears to be in good agreement with experimental data from an air jet impinging on a solid surface (e.g., [22,39]), Phares et al. [23] pointed out an inconsistency in its derivation. The equation of motion was solved in the axial direction for the impingement region, but the wall shear stress, which is in the radial direction, was mistakenly defined based on that solution. It appears serendipitous then that the maximum shear stress relation (Eq. 13) as an empirical relation based on the stated experimental results holds within 15 % of the observed data. Those data were measured using a Preston tube with an outside diameter of 1.2 mm calibrated in fully developed turbulent shear flows, and Phares et al. [23] explained that the severe pressure gradients in the impingement region laminarize the boundary layer and so the Preston tube cannot be used to measure shear stress within the impingement region.

Solving the boundary layer equation in the radial direction along the surface, Phares et al. [23] derived a model to find the wall shear stress for the laminar boundary layer of an axisymmetric fully-developed jet as

$$\frac{\tau}{\rho U_0^2} \text{Re}_0^{1/2} \left(\frac{H}{d_0} \right)^2 = g_2 \left(\frac{r}{H} \right) \quad (15)$$

where $\text{Re}_0 = U_0 d_0 / \nu$ is the Reynolds number based on jet discharge values, ν is kinematic viscosity, and g_2 is a universal function. Based on this model, the magnitude τ_m and location r_m of the shear stress peak are

$$\tau_m = 44.6 \rho U_0^2 \text{Re}_0^{-1/2} \left(\frac{H}{d_0} \right)^{-2}, \quad \frac{r_m}{H} = 0.09 \quad (16)$$

For the turbulent boundary layer, Poreh et al. [46] empirically developed the wall shear stress distribution as

$$\frac{\tau}{\rho U_0^2} \text{Re}_0^{1/2} \left(\frac{H}{d_0} \right)^2 = 0.34 \text{Re}_0^{1/5} \left(\frac{r}{H} \right)^{-2.3} \quad (17)$$

Figure 14 shows that the measured turbulence intensities $\left(I = \frac{\sqrt{u'^2 + v'^2}}{\sqrt{u^2 + v^2}} \right)$ near the wall are relatively high with a peak at the impingement point. Based on the law of the wall [64], there is a very thin viscous sublayer very close to the wall where the velocity distribution is linear

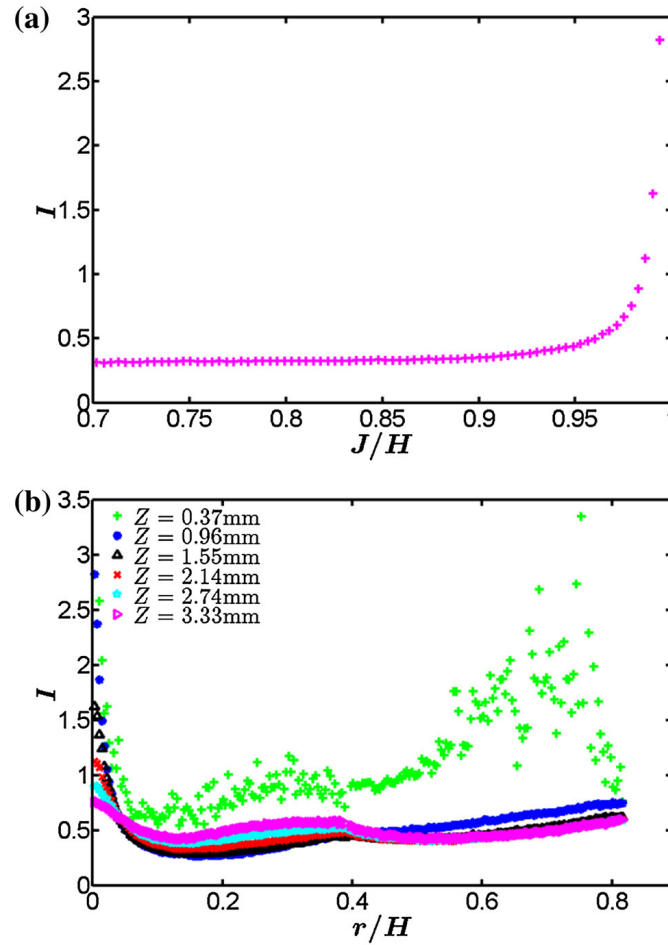


Fig. 14 Turbulence intensity (a) at jet centerline along the free jet axis, and (b) in the vicinity of the impingement wall

and the viscous shear stress can be computed based on the slope of this line. Results of the wall jet velocity distribution (Fig. 7a) show that this layer is very thin, such that the local maximum radial velocities occur at the second closest measurement position to the wall (1 mm above the wall) and the velocities at the closest position to the wall (0.4 mm above the wall) are, on average, 53 % of the local maximum value until $r/H = 0.27$. It should be noted that measurements within this layer are difficult to obtain. In this study, the wall shear stress is determined using two methods.

First, Reynolds shear stress ($\rho \overline{u'v'}$) was computed above the wall and linearly extrapolated to the wall. As discussed above, measured near-wall values of $\rho \overline{u'v'}$ did not show a reasonable trend and exhibited oscillations between negative and positive values (Fig. 8d). To avoid any errors in data very close to the bed, the extrapolation was done using two reliable points. The first point is the location of local maximum value of absolute Reynolds stress. Note that the Reynolds stress at this point is negative by convention. This local maximum occurs 1.5 mm above the bed in the vicinity of the impingement point, and then this distance increases almost linearly, reaching 11 mm at $r/H = 0.82$ (Fig. 8a). The second point is the location of local maximum radial velocity, where by definition the total shear stress is zero. Thus, the line

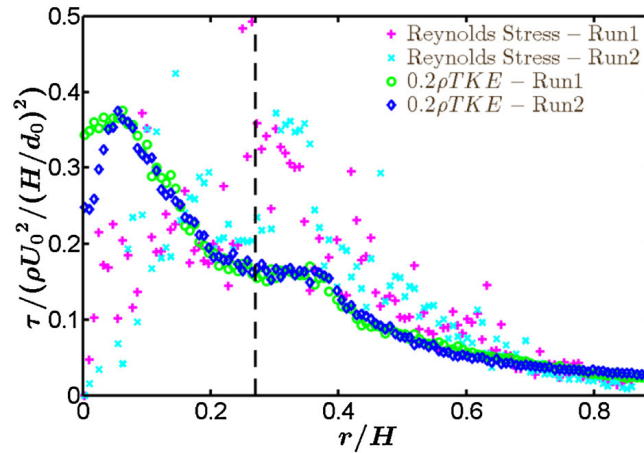


Fig. 15 Dimensionless wall shear stress based on extrapolation of Reynolds stress and *TKE* (dashed line to the left is the impingement region and to the right is the wall jet region)

that passes through these two points is projected to the bed to find the total wall shear stress. For the second method, Haehnel and Dade [2] showed that for an axisymmetric impinging jet, $\overline{u'v'} = 0.2TKE$ where $TKE = 0.5 (\overline{u'^2} + \overline{v'^2} + \overline{w'^2})$ is turbulent kinetic energy per unit mass. Here, two-dimensional velocities were measured on a plane passing through the jet axis, so shear stress at the bed was determined using $TKE = 0.5 (\overline{u'^2} + \overline{v'^2})$, and it was assumed that the angular component of velocity fluctuations ($\sqrt{\overline{w'^2}}$) is negligible. Thus, *TKE* values were extrapolated linearly to the bed to estimate wall shear stress.

Both of these methods give almost the same distributions of wall shear stress for $r/H \geq 0.5$ (Fig. 15). These distributions, however, differ markedly for $r/H < 0.5$, although the maxima are almost the same. Results of the first method depend highly on the accuracy of the location of the local maximum velocity, but there is some uncertainty in its accuracy because of the resolution of measurements close to the impingement plane. As noted, the local maximum velocity occurs less than 1 mm from the wall in the region from the impingement point to $r/H = 0.24$, while the data resolution is 0.6 mm in this region. The second method, however, extrapolates the *TKE* using four data points near the wall other than the one closest to the wall to determine the corresponding values on the wall. The accuracy of this method is higher than for the first method as more points are used for the extrapolation and the accuracy of extrapolation is not highly dependent on data resolution.

While most of the proposed distributions under an impinging jet show zero wall shear stress at the impingement point, the literature indicates that the erosion rate at the jet centerline is, in fact, not zero. Zero shear stress on a surface implies no sediment erosion. Thus, the shear stress distribution of Beltaos and Rajaratnam ([22]; Eq. 12) makes little physical sense close to the jet centerline, where on a soil bed the maximum scour hole depth forms (e.g., [13, 65]). The calculated distributions of shear stress for both Runs 1 and 2 show a non-zero value at $r/H = 0$, which is more physically consistent with maximum erosion that takes place at that point. Based on the JET method, the critical shear stress is defined assuming a linear relationship between erosion rate and shear stress at the impingement point [13]. While Hanson and Cook [13] assumed maximum shear stress causes the maximum scour hole at the impingement point, the applied distribution of wall shear stress shows a zero value right at $r/H = 0$. Although the maximum shear stress based on the *TKE* distribution

is not at $r/H = 0$, it would partially justify the maximum erosion at that point by showing a high value at $r/H = 0$ (Fig. 15). It would be useful to note that high mean pressure and also high fluctuations of pressure near the impingement plane especially at the impingement point could be considered as another driver of erosion [66]. Hence, the assumption of linear relationship between erosion rate and shear stress may not be valid at the impingement point.

The position of the peak shear stress based on the Reynolds stress occurs at a greater distance from the jet centerline (impingement point) in comparison to the distribution based on *TKE*. Haehlen and Dade's [2] experiments determined the peak erosion rate location at about $r/H = 0.1$ for $H/d_0 = 154.2$, similar to the location of peak wall shear stress at $r/H = 0.14$ reported by Beltaos and Rajaratnam [22]. In this study, the peak shear stress occurred at $r/H = 0.06$ based on *TKE* and $r/H = 0.30$ based on Reynolds stress. The lower entrainment and lateral spreading rate of the free jet result in a thinner free jet in comparison to those formed in unconfined conditions. When a thinner jet impinges on the wall, the peak of the shear stress should occur at a smaller radial distance from the impingement point. This result agrees well with the wall shear stress based on *TKE*. There is good consistency between measured spreading rate of the free jet and position of the peak shear stress based on *TKE*. The spreading rate of the free jet is about 33 % less than previously reported values, and the wall shear stress peak, based on *TKE*, occurs about 33 % closer to the nozzle in comparison to the wall shear stress distribution of Phares et al. [23].

The peak values of the shear stress distributions found here are more than 2.4 times larger than those of Eq. (13). Values of C_s were found to be 0.38 for both Runs 1 and 2, respectively, in comparison to the value of 0.16 proposed by Beltaos and Rajaratnam [22]. As previously discussed, their wall shear stress distribution appears theoretically invalid. The peaks of Run 1 and Run 2 are, respectively, 28 and 53 % higher than the corresponding values in Phares et al. [23] distribution. It appears that jet confinement affects the shear stress distribution on the wall by decreasing the entrainment of fluid and by increasing the momentum transfer. This increased momentum accumulates in the relatively thin impinging jet and significantly increases the maximum shear stress exerted on the wall in comparison to the distributions predicted by Phares et al. [23] from the jet centerline up to a radial distance of about $0.4H$ (Fig. 16). The error bars on Fig. 16 are the 95 % confidence level for the extrapolation of *TKE* to the impingement wall. The confidence levels show that there is a meaningful difference between shear stress in the confined condition and all other relations for unconfined conditions for $r/H < 0.4$.

There are several differences in the shear stress distribution based on *TKE* for Run 1 and Run 2 close to the impingement point. These differences might be due to the nozzle velocity. Since a wide range of nozzle velocities was not tested, no conclusion about the impact of this variable can be drawn. The distribution of shear stress in Run 2 is chosen for further analysis as its nozzle velocity was higher than for Run 1 and the distribution of shear stress appears better developed. To fit a curve through this distribution, the shear stress results based on *TKE* are divided into two zones: from $r/H = 0$ to 0.38, and $r/H > 0.38$ (Fig. 16). In the first zone, shear stress increases from a value of about 65 % of the maximum at the jet centerline to the maximum at $r/H = 0.06$, and it then decreases to a value of about 41 % of the maximum at $r/H = 0.38$. It is interesting to note that high values of shear stress between $r/H = 0$ and 0.19 physically correspond to the lateral extent of the free jet since the free jet full-width right before entering the impingement region is slightly less than $5d_0$ ($\approx 0.20H$; see Fig. 10) for the right side of the jet. A curve can be fitted through data between $r/H = 0$ and 0.38 with $R^2 \cong 0.99$,

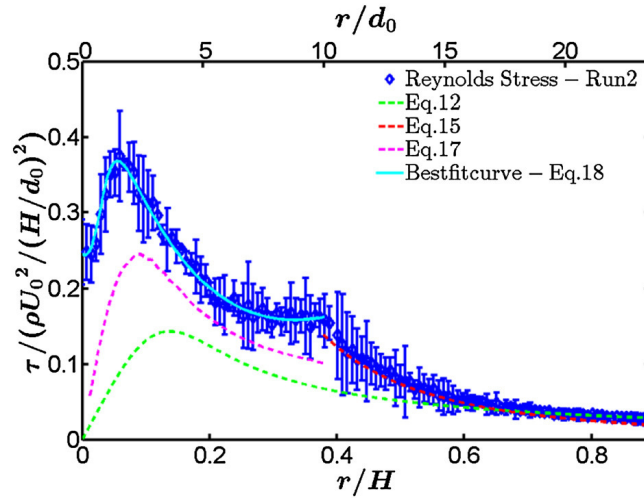


Fig. 16 TKE-based shear stress compared to literature shear stress distributions and best fit curve. The error bars shows the 95 % confidence level for the extrapolation of TKE to the impingement wall

$$\frac{\tau_m}{\rho U_0^2 \left(\frac{H}{d_0}\right)^{-2}} = \frac{0.303}{1 + 11.26e^{-87.1\lambda}} - 2.632\lambda e^{-3.067\lambda^{1.14}} + 0.220 \quad (18)$$

Between $r/H = 0.19$ and 0.38 , the shear stress variation is low. In this zone, the radial velocity strongly decreases (see Fig. 7c) while the wall jet width is slowly increasing (see Fig. 7b), so it makes physical sense to have a low variation in the shear stress in this region. In the region $r/H > 0.38$, the shear stress distribution follows that of Poreh et al. [46], but with slightly higher values (about 13 % greater on average).

4.3 Implications for sediment erodibility assessment

As previously noted, the JET is an ASTM standard used for sediment erodibility assessment in the field, and the results presented here address an important aspect of the analytical method developed by Hanson and Cook [13], which is the effect of confinement on bed shear stress at impingement. The method developed by Hanson and Cook is based on the presumption that the shear stress distribution of an impinging jet within the apparatus is identical to that observed in unconfined conditions. This study shows unequivocally that confinement can significantly alter the maximum value of this shear stress and its radial distribution from the impingement location. While the maximum shear stress for the conditions of this study and the particular confinement ratio was about 240 % higher than the value based on the JET methodology, the maximum shear stress is expected to be affected by the confinement ratio. Recently, a miniature version of the JET device (“mini” JET) was developed for easier use in field applications, and this device was compared to the original JET [29, 67]. The “mini” JET is smaller and lighter than the original jet and has a smaller nozzle diameter (3.2 mm) and cylindrical tank diameter (about 0.1 m) as compared to the original JET (6.4 mm and 0.3 m, respectively). Note that the cylindrical tanks of the original and “mini” JET apparatuses are much smaller than the box used in the present study, so the effect of confinement is expected to be more severe for the JET. Al-Madhhachi et al. [29] compared the erodibility of carefully prepared sediment samples using both the original JET and the “mini” JET. They found that the soil’s measured erodibility coefficient k_d was the same between the original

and the “mini” JET, but the critical shear stress τ_c as determined using the “mini” JET was significantly lower (more than an order of magnitude lower) than that derived for the original JET. Al-Madhhachi et al. hypothesized that this difference in τ_c was due to the scales of the jet nozzles and the compaction method, and therefore introduced an adjustment coefficient to match the critical shear stress from the “mini” JET to the one from the original JET. Based on the results presented herein, it is more likely that the assumed shear stresses within both the original and “mini” JET devices on the sample surface are not equivalent. As noted above, the JET methodology under predicts the applied shear stress in the original apparatus due to the effects of confinement. The apparent discord between the original JET and the “mini” JET, i.e., the severe under prediction of the critical shear stress of the soil, likely is due to the stronger confinement conditions. Note that the confinement ratio of the “mini” JET is about 1,020, compared to the value of about 2,270 for the original JET. It is hypothesized here that the observed differences in the original and “mini” JET test results are due to the confinement effects.

The size of the resultant scour hole created by the JET apparatus also might affect the shear stress distribution. Weidner [24] showed that for wide and shallow scour holes, the effect of scour hole shape on the shear stress distribution of the jet inside the hole is negligible. Thus, the maximum wall shear stress in these conditions can be found using the flat surface shear stress distribution (Eq. 18),

$$\tau_m = C_s \frac{\rho U_0^2}{(H_e/d_0)^2} \quad (19)$$

where C_s is the shear stress coefficient and H_e is the initial impingement height plus the scour hole depth. For the confined conditions presented here, C_s is 0.38. The stronger confinement of the JET apparatuses is expected to increase wall shear stresses and increase values of C_s in Eq. 19, with C_s for the “mini” JET being greater than for the original JET.

5 Conclusions

The hydrodynamics of an axisymmetric impinging jet commonly employed to assess sediment erodibility were investigated using PIV in a laboratory tank. The PIV apparatus was able to measure the velocity in both the near- and far-field regions of the free and wall jet, and these measurements agree well with the general behavior of impinging jets described in the literature. Mean and turbulent velocities follow self-similarity profiles in the free jet and wall jet region. Two major phenomena were observed in the confined conditions: (1) low entrainment because of limited source of fluid to be entrained into the jet, and (2) an increased rate of momentum transfer in the free jet because of the added momentum by the secondary flow. These two phenomena appear to play key roles in modifying the behavior of a confined jet in comparison to a jet in unconfined conditions. For example, the axial diffusion coefficient C_d was found to be a function of nozzle velocity and on average about 20 % higher than previously reported. The lateral spreading rate also was found to be a function of nozzle velocity and on average was 33 % lower than previously reported values. This low-spread jet with high diffusion in the axial direction altered the shear stress distribution at and downstream of the impingement point.

Wall shear stress was found based on the extrapolation of Reynolds stress and *TKE*. Using *TKE* to estimate shear stress showed a more consistent distribution as compared to other observations, particularly since it resulted in non-zero shear stress at the impingement point, which is typically where maximum erosion is observed. Based on *TKE*, the maximum wall

shear stress occurred 33 % closer to the impingement point, and with 240 % higher values, in comparison to the standard values recommended for use in the JET methodology. A semi-empirical equation (Eq. 19) was developed to predict the applied shear stress by the JET in the field. The value of shear stress coefficient C_s in this equation should be reevaluated for the confined conditions of the original and “mini” JETs. Since these apparatuses are cylindrical and much smaller than the box in these experiments, the impact of jet confinement may be expected to be even more severe for the JETs. The present findings hypothesize confinement effects as the reason for observed inconsistencies between the “mini” and original JETs, and redefining the apparatus coefficients and relations should improve soil and sediment erosion assessment in the field. Further studies are needed to understand those effects in the actual conditions of the jet devices, to compute or measure the shear stress in the boundary layer with higher resolution to eliminate the errors induced by extrapolations, and to examine the role of pressure on erosion of sediment near the location of jet impingement.

Acknowledgments This research benefitted greatly from discussions with Robert Wells, and by the constructive reviews of two anonymous referees. We also thank Kevin Cullinan for technical support. This work was partially supported by NSF-EAR 0549607 and the USDA-ARS (Specific Research Agreement No. 58-6408-9-346).

References

- Bennett SJ, Alonso CV (2005) Kinematics of flow within headcut scour holes on hillslopes. *Water Resour Res* 41:1–12. doi:[10.1029/2004WR003752](https://doi.org/10.1029/2004WR003752)
- Haehnel R, Dade W (2008) Physics of particle entrainment under the influence of an impinging jet. US Army Corp, Cold Regions Research and Engineering Laboratory, Hanover
- Gholamreza-Kashi S, Martinuzzi R (2007) Mean flow field of a nonbuoyant rectangular surface jet. *J Hydraul Eng* 133:234–239. doi:[10.1061/\(ASCE\)0733-9429\(2007\)133:2\(234\)](https://doi.org/10.1061/(ASCE)0733-9429(2007)133:2(234))
- Moore WL, Masch FD (1962) Experiments on the scour resistance of cohesive sediments. *J Geophys Res* 67(4):1437–1449
- Hollick M (1976) Towards a routine test for the assessment of the critical tractive forces of cohesive soils. *Trans Am Soc Agric Biol Eng* 19:1076–1081
- Hanson GJ, Robinson KM (1993) The influence of soil moisture and compaction on spillway erosion. *Trans Am Soc Agric Biol Eng* 36:1349–1352
- Mazurek KA, Rajaratnam N, Sego DC (2001) Scour of cohesive soil by submerged circular turbulent impinging jets. *J Hydraul Eng* 127:598–606
- Haehnel RB, Dade WB, Cushman-Roisin B (2008) Crater evolution due to a jet impinging on a bed of loose particles. In: *Proceeding Earth Sp. 2008*. American Society of Civil Engineers, Reston, 1–10
- Haehnel R, Dade WB (2010) Particle entrainment by non-uniform Eolian flow. In: *Proceeding Earth Sp. 2010*. American Society of Civil Engineers, Reston, 158–165
- Hogg AJ, Dade WB, Huppert HE, Soulsby RL (1996) A model of an impinging jet on a granular bed, with application to turbulent, event-driven bedload transport. In: Ashworth PJ, Bennett SJ, Best JL, McLelland S (eds) *Coherent flow structures in open channels*. Wiley, New York, pp 101–124
- Tolhurst TJ, Black KS, Shayler SA (1999) Measuring the in situ erosion shear stress of intertidal sediments with the cohesive strength meter (CSM). *Estuar Coast Shelf Sci* 49:281–294
- Hanson G (1990) Surface erodibility of earthen channels at high stresses. Part II—developing an in situ testing device. *Trans Am Soc Agric Biol Eng* 33:132–137
- Hanson G, Cook K (2004) Apparatus, test procedures, and analytical methods to measure soil erodibility in situ. *Appl Eng Agric* 20:455–462
- ASTM Standard “D5852” (1995) Standard test method for erodibility determination of soil in the field or in the laboratory by the jet index method. doi:[10.1520/D5852-00R07](https://doi.org/10.1520/D5852-00R07), www.astm.org
- Kamphuis JW, Hall KR (1983) Cohesive material erosion by unidirectional current. *J Hydraul Eng* 109:49–61. doi:[10.1061/\(ASCE\)0733-9429\(1983\)109:1\(49\)](https://doi.org/10.1061/(ASCE)0733-9429(1983)109:1(49))
- Rohan K, Lefebvre G, Douville S, Milette J (1986) A new technique to evaluate erosivity of cohesive material. *ASTM Geotech Test J* 9:87–92

17. McNeil J, Taylor C, Lick W (1996) Measurements of erosion of undisturbed bottom sediments with depth. *J Hydraul Eng* 122:316–324. doi:[10.1061/\(ASCE\)0733-9429\(1996\)122:6\(316\)](https://doi.org/10.1061/(ASCE)0733-9429(1996)122:6(316))
18. Briaud J, Ting F, Chen H (2001) Erosion function apparatus for scour rate predictions. *J Geotech Geoenvironmen Eng* 127:105–113
19. Hanson GJ, Simon A (2001) Erodibility of cohesive streambeds in the loess area of the midwestern USA. *Hydrol Process* 15:23–38. doi:[10.1002/hyp.149](https://doi.org/10.1002/hyp.149)
20. Hanson G, Robinson K, Cook K (2002) Scour below an overfall: Part II. Prediction. *Trans Am Soc Agric Biol Eng* 45:957–964
21. Mercier F, Bonelli S, Pinettes P, et al (2013) Comparison of CFD simulations with experimental jet erosion tests results. *J Hydraul Eng*. doi:[10.1061/\(ASCE\)HY.1943-7900.0000829](https://doi.org/10.1061/(ASCE)HY.1943-7900.0000829)
22. Beltaos S, Rajaratnam N (1974) Impinging circular turbulent jets. *J Hydraul Div* 100:1313–1328
23. Phares DJ, Smedley GT, Flagan RC (2000) The wall shear stress produced by the normal impingement of a jet on a flat surface. *J Fluid Mech* 418:351–375. doi:[10.1017/S002211200000121X](https://doi.org/10.1017/S002211200000121X)
24. Weidner KL (2012) Evaluation of the Jet Test Method for determining the erosional properties of Cohesive Soils; A Numerical Approach. MS thesis, Virginia Polytechnic Institute and State University, Blacksburg
25. Hanson G, Robinson K, Temple D (1990) Pressure and stress distributions due to a submerged impinging jet. In: *Proceeding of ASCE National Conference Hydraulic Engineering*, San Diego, 525–530
26. Willert C (1997) Stereoscopic digital particle image velocimetry for application in wind tunnel flows. *Meas Sci Technol* 8:1465–1479. doi:[10.1088/0957-0233/8/12/010](https://doi.org/10.1088/0957-0233/8/12/010)
27. Albertson ML, Dai YB, Jensen RA, Rouse H (1950) Diffusion of submerged jets. *Trans Am Soc Civ Eng* 115:639–664
28. Kwon SJ, Seo IW (2005) Reynolds number effects on the behavior of a non-buoyant round jet. *Exp Fluids* 38:801–812. doi:[10.1007/s00348-005-0976-6](https://doi.org/10.1007/s00348-005-0976-6)
29. Al-Madhhachi A, Hanson G, Fox G et al (2013) Measuring soil erodibility using a laboratory “mini” JET. *Trans Am Soc Agric Biol Eng* 56:901–910
30. Daily JW, Harleman DRF (1966) *Fluid dynamics*. Addison-Wesley, New York
31. Hussein HJ, Capp SP, George WK (1994) Velocity measurements in a high-Reynolds-number, momentum-conserving, axisymmetric, turbulent jet. *J Fluid Mech* 258:31–75
32. Papanicolaou P (1984) Mass and momentum transport in a turbulent buoyant vertical axisymmetric jet. Ph.D. Thesis, Division of Engineering and Applied Science, California Institute of Technology, Pasadena, CA
33. George W (1989) The self-preservation of turbulent flows and its relation to initial conditions and coherent structures. *Adv Turbul* 39–73
34. Liu H, Winoto SH, Shah DA (1997) Velocity measurements within confined turbulent jets: application to cardiovascular regurgitation. *Ann Biomed Eng* 25:939–948
35. Rajaratnam N (1976) *Turbulent jets*. Elsevier Science Publishing Co, Amsterdam
36. Xu G, Antonia R (2002) Effect of different initial conditions on a turbulent round free jet. *Exp Fluids* 33:677–683. doi:[10.1007/s00348-002-0523-7](https://doi.org/10.1007/s00348-002-0523-7)
37. Papanicolaou PN, List EJ (1988) Investigations of round vertical turbulent buoyant jets. *J Fluid Mech* 195:341–391
38. Hongwei W (2000) Investigations of buoyant jet discharges using combined DPIV and PLIF. Dissertation, Nanyang Technological University
39. Bradshaw P, Love E (1961) The normal impingement of a circular air jet on a flat surface. *ARC Rep Memo* 3205(1):8
40. Tani I, Komatsu Y (1964) Impingement of a round jet on a flat surface. In: *Proceeding 11th International Congress Applied Mechanics Munich, Germany*, 672–676
41. Rajaratnam N, Zhu DZ, Rai SP (2010) Turbulence measurements in the impinging region of a circular jet. *Can J Civ Eng* 37:782–785. doi:[10.1139/L10-014](https://doi.org/10.1139/L10-014)
42. Rajaratnam N, Mazurek K (2005) Impingement of circular turbulent jets on rough boundaries. *J Hydraul Res* 43:689–695
43. Kataoka K, Mizushima T (1974) Local enhancement of the rate of heat-transfer in an impinging round jet by free-stream turbulence. *Proc Fifth Int Heat Transf Conf Tokyo* 2:305–309
44. Beltaos S, Rajaratnam N (1977) Impingement of axisymmetric developing jets. *J Hydraul Res* 15:311–326
45. Poreh M, Cermak JE (1959) Flow characteristics of a circular submerged jet impinging normally on a flat boundary. In: *Sixth Midwestern Conference on Fluid Mechanics Austin, Texas*, 198–212
46. Poreh M, Tsuei YG, Cermak JE (1967) Investigation of a turbulent radial wall jet. *J Appl Mech* 34:457–463
47. Verhoff A (1963) The two-dimensional turbulent wall jet with and without an external stream. Report No. 626, Office of Naval Research, Washington, DC
48. Karimipناه T (1996) Turbulent jets in confined spaces. Dissertation, Centre for Built Environment, Royal Institute of Technology

- 715 49. Ricou FP, Spalding DB (1961) Measurements of entrainment by axisymmetrical turbulent jets. *J Fluid*
- 716 *Mech* 11:21–32
- 717 50. Kaminski E, Tait S, Carazzo G (2005) Turbulent entrainment in jets with arbitrary buoyancy. *J Fluid Mech*
- 718 526:361–376. doi:[10.1017/S0022112004003209](https://doi.org/10.1017/S0022112004003209)
- 719 51. Fischer HB, List EJ, Koh RCY (1979) *Mixing in inland and coastal waters*. Academic Press, New York
- 720 52. Baydar E, Ozmen Y (2006) An experimental investigation on flow structures of confined and unconfined
- 721 impinging air jets. *Heat Mass Transf* 42:338–346. doi:[10.1007/s00231-005-0021-6](https://doi.org/10.1007/s00231-005-0021-6)
- 722 53. Schafer DM, Ramadhani S, Incropera FP (1992) Numerical simulation of laminar convection heat
- 723 transfer from an in-line array of discrete sources to a confined rectangular jet. *Numer Heat Transf Part A*
- 724 *Appl* 22:121–141. doi:[10.1080/10407789208944762](https://doi.org/10.1080/10407789208944762)
- 725 54. Chalupa R, Chen M, Modi V, West AC (2001) High Schmidt mass transfer in a turbulent impinging
- 726 slot-jet flow. *Int J Heat Mass Transf* 44:3775–3785. doi:[10.1016/S0017-9310\(01\)00042-4](https://doi.org/10.1016/S0017-9310(01)00042-4)
- 727 55. Ashforth-Frost S, Jambunathan K, Whitney CF (1997) Velocity and turbulence characteristics of
- 728 a semiconfined orthogonally impinging slot jet. *Exp Therm Fluid Sci* 14:60–67. doi:[10.1016/S0894-1777\(96\)00112-4](https://doi.org/10.1016/S0894-1777(96)00112-4)
- 729 56. Fitzgerald JA, Garimella SV (1997) Flow field effects on heat transfer in confined jet impingement. *J*
- 730 *Heat Transf* 119:630–632. doi:[10.1115/1.2824152](https://doi.org/10.1115/1.2824152)
- 731 57. Obot NT, Douglas WJM, Mujumdar AS (1982) Effect of semi-confinement on impingement heat transfer.
- 732 *Proc Heat Transf* 1982:395–400
- 733 58. Cape EG, Skoufis EG, Weyman AE (1989) A new method for noninvasive quantification of valvular
- 734 regurgitation based on conservation of momentum. In vitro validation. *Circulation* 79:1343–1353. doi:[10.1161/01.CIR.79.6.1343](https://doi.org/10.1161/01.CIR.79.6.1343)
- 735 59. Karimipناه MT, Sandberg M (1994) Decay of momentum and velocity in an axisymmetric impinging
- 736 jet. In: *Proceedings of the Fourth International Conference of Air Distribution in Rooms*
- 737 60. Karimipناه MT, Sandberg M (1994) Deflection and influence of room-size of a two-dimensional wall
- 738 jet in a ventilated room. In: *Proceedings of the Fourth International Conference of Air Distribution in*
- 739 *Rooms*
- 740 61. Abrahamsson H, Johansson B, Löfdahl L (1994) A turbulent two-dimensional wall-jet in a quiescent
- 741 surrounding. *Eur J Mech* 13:533–556
- 742 62. Malmström T, Christensen B, Kirkpatrick A (1992) Low velocity air jets from round nozzles. *Jets Round*
- 743 *Nozzles* 245:643–668
- 744 63. George WK (1990) Governing equations, experiments, and the experimentalist. *Exp Therm Fluid Sci*
- 745 3:557–566. doi:[10.1016/0894-1777\(90\)90071-E](https://doi.org/10.1016/0894-1777(90)90071-E)
- 746 64. Von Karman T (1930) *Mechanical Similitude and Turbulence*. Translated by National Advisory Commit-
- 747 tee for Aeronautics TM611 (originally Publ. Ger)
- 748 65. Cossette D, Mazurek KA, Rennie CD (2012) Critical Shear Stress from Varied Method of Analysis of a
- 749 Submerged Circular Turbulent Impinging Jet Test for Determining Erosion Resistance of Cohesive. 6th
- 750 International Conference on Scour and Erosion. Paris, 11–18
- 751 66. Vollmer S, Kleinhans MG (2007) Predicting incipient motion, including the effect of turbulent pressure
- 752 fluctuations in the bed. *Water Resour Res*. doi:[10.1029/2006WR004919](https://doi.org/10.1029/2006WR004919)
- 753 67. Daly ER, Fox GA, Al-Madhhachi AT, Miller RB (2013) A scour depth approach for deriving erodibility
- 754 parameters from jet erosion tests. *Trans ASABE* 56:1343–1351. doi:[10.13031/trans.56.10350](https://doi.org/10.13031/trans.56.10350)
- 755
- 756